Biodegradation behaviour of Fe-based alloys in Hanks' Balanced Salt Solutions: Part II. The evolution of local pH and dissolved oxygen concentration at metal interface

Cheng Wang [a,*], Christabelle Tonna [b], Di Mei [a,c], Joseph Buhagiar [b], Mikhail L. Zheludkevich [a,d], Sviatlana V. Lamaka [a]

[a] *Institute of Surface Science, Helmholtz-Zentrum Hereon, Geesthacht, 21502, Germany*
[b] *Department of Metallurgy and Materials Engineering, University of Malta, Msida, Malta*
[c] *School of Materials Science and Engineering & Henan Key Laboratory of Advanced Magnesium Alloy, Zhengzhou University, Zhengzhou, 450001, PR China*
[d] *Institute for Materials Science, Faculty of Engineering, Kiel University, Kiel, 24103, Germany*

ARTICLE INFO

ABSTRACT

Commercially pure Fe, Fe35Mn, and (Fe35Mn)5Ag alloys were prepared by uniaxial pressing of the mixture of individual powders, followed by sintering. The influence of the alloying elements Mn and Ag on the corrosion behaviour of these Fe-based alloys was investigated in Hanks' Balanced Salt Solution (HBSS). Furthermore, the role of the components in HBSS, particularly Ca^{2+} ions during alloys degradation was studied. Distribution of local pH and dissolved oxygen concentration was measured 50 μm above the interface of the degrading alloys. The results revealed that 5 wt% Ag addition to Fe35Mn alloy triggered micro-galvanic corrosion, while uniform corrosion dominated in pure Fe and Fe35Mn. Fast precipitation of Ca–P-containing products on the surface of these Fe-based alloys buffered local pH at the metal interface, and blocked oxygen diffusion at the initial stages of immersion. In the (Fe35Mn)5Ag, the detachment or structural changes of Ca–P-containing products gradually diminished their barrier property. These findings provided valuable insights into the degradation mechanism of promising biodegradable Fe-based alloys.

1. Introduction

Iron-based biodegradable materials have recently been proposed as promising candidates for biodegradable medical implants, especially for orthopaedic and cardiovascular applications, owing to their favourable mechanical properties [1]. However, slow degradation rate and detrimental ferromagnetism *in vivo* restrict pure Fe's biomedical applications [2]. Due to this, multiple efforts have been made over the past few years to enhance the biodegradation and improve the biocompatibility of Fe-based alloys, involving alloying Fe with various elements. Mn, a trace element found in human body that acts as an indispensable cofactor of numerous diverse enzymes, has been considered as a suitable alloying element. Several studies have shown that Mn addition has the tendency to increase the degradation rate and also eliminates the ferromagnetic nature of the metal through the formation of an antiferromagnetic austenitic microstructure [3–6].

Although it is undisputed that Mn addition could eliminate the ferromagnetic nature of Fe, there have been conflicting conclusions with regards to its ability to facilitate biodegradation. The variation in the degradation rate of Fe–Mn alloys remains highly dependent on Mn concentration and resulting microstructure. Hermawan et al. [3] pioneered several investigations on biodegradable Fe–Mn alloys and found that the degradation rate of Fe–Mn alloys decreased with incrementation of Mn concentration from 20 wt% to 35 wt%. This is due to the bi-phasic microstructures that triggered additional micro-galvanic corrosion [7–13]. By contrast, no significant corrosion was observed during long-term *in vivo* tests of Fe–Mn alloy (Mn < 10%) [14]. It has been also reported that Fe–30Mn alloy degraded slower than pure Fe during static immersion, notwithstanding the expected higher corrosion rates of Fe–30Mn calculated from potentiodynamic tests [15]. Similar outcomes have been obtained by Čapek, Kubásek, Vojtěch, Jablonská, Lipov and Ruml [16], who manufactured a hot-forged Fe–30Mn alloy
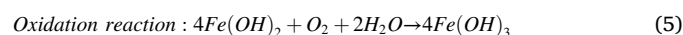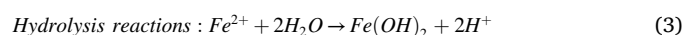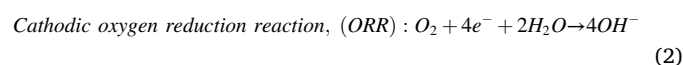
and observed lower corrosion rates for Fe–Mn system compared to pure Fe in both Simulated Body Fluid (SBF) and Dulbecco's Modified Eagle's Medium (DMEM). They attributed these results partly to the fact that the experimental conditions for immersion tests were not identical to those used in potentiodynamic tests, where insufficient exposure of medium to metal limited the formation of protective compounds on the surface. Čapek, Kubásek, Vojtěch, Jablonská, Lipov and Ruml [16] also discussed how the higher solubility of Mn hydroxides, compared to Fe hydroxides, may have led to higher pH levels adjacent to the sample surface, leading to a decelerated cathodic reaction and preferential formation of products like $Fe(OH)_2$ and $Fe(OH)_3$. There has also been varying observations on the composition and structure of the degradation products on Fe–Mn alloys. Moreover, Dargusch, Dehghan-Manshadi, Shahbazi, Venezuela, Tran, Song, Liu, Xu, Ye and Wen [17] claimed that the corrosion rates of Fe–Mn alloys increased with increments in Mn content while the corrosion rates derived from potentiodynamic curves were consistent with those obtained from the immersion tests. They also pointed out that while the presence of Fe and Mn oxides post degradation had been consistent across various studies [11,12,14,17–23], the presence of Fe/Mn phosphates, has not been consistently observed despite the mention of phosphorus among detected elements in corrosion products [5,14]. The state-of-art on the degradation of Fe–Mn alloys reviewed here clearly highlights that there is a lacuna of knowledge in the field. It is for this reason that the influence of Mn addition as an alloying element to create an Fe–Mn based alloy on degradation needs further investigation. The use of advanced techniques that can monitor the evolution of local pH and dissolved oxygen (DO) and help uncover the underlying degradation mechanism of Fe–Mn alloys in electrolytes like Hanks' Balanced Salt Solution (HBSS).

The addition of immiscible noble elements (e.g. palladium, silver, gold) within the microstructure of Fe and its alloys is another strategy to further increase the degradation rate. In this case, second phases of these noble metals within the Fe-based matrix are formed and promote micro-galvanic couples [21]. To illustrate this, it has been reported that alloying Fe with Pd accelerated the corrosion rate of Fe in SBF [24,25]. Schinhammer et al. [26] evaluated the degradation performance of Fe–Mn–C(-Pd) alloys in SBF and found that while the Fe–Mn–C(-Pd) alloys degraded faster than the metal without the Pd addition, the degradation rate decreased with immersion time because of the gradual growth of degradation products. Huang et al. [27] implanted silver ions into pure Fe through metal vapour vacuum arc techniques and noticed uniform corrosion following immersion testing. Furthermore, a biodegradable Fe–Mn–Ag alloy was designed with accelerated corrosion rate and appropriate antibacterial characteristics. Even though alloying with noble elements was shown to increase the corrosion rate of Fe-base alloy in test media, less significant enhancements have been achieved on their *in vivo* degradation rate [28,29]. Meanwhile, preferential precipitation of phosphates was observed on the noble phases, which experience higher alkalinisation owing to the oxygen reduction reaction (ORR) occurring on these cathodic sites [30]. Moreover, one of the issues uncovered from an *in vivo* test on Fe–Mn–C(-Pd) seems to be, the lack of dissolved oxygen available at certain implantation sites [2], showing that it is indispensable to deepen understanding of oxygen consumption at degrading surfaces *in vitro*. Apart from this, large inconsistencies between *in vivo* and *in vitro* results are likely due to discrepancies of components in pseudo-physiological media and testing conditions compared to the actual implantation environment. This highlights the importance of understanding the influence of the electrolyte components (e.g. Ca^{2+}) and testing conditions to gain more representative information regarding the degradation behaviour of biodegradable metals.

Apart from material composition, processing techniques also have a significant impact on the material's degradation performance. Powder processing has consistently been a popular processing technique for the preparation of biodegradable implant materials. Its applicability has been exploited for the preparation of cardiovascular stents [6,31] and porous scaffold structures using more flexible methods like the space-holder technique [23], the replication method [12,32,33] and recent novel techniques involving pressureless microwave sintering [34] and extrusion-based 3D printing [35]. The fundamental difference in powder-processing microstructures and microstructures prepared using melt processing, is the resultant porosity in the former. To this effect, multiple groups have confirmed the increase in degradation resulting from increased percentage porosity in the tested samples [23,36,37]. Apart from this, powder-processed metal, especially FeMn-based alloys of interest in the field, are more susceptible to the formation of manganese oxide inclusions resulting from high temperature oxidation [38]. The exact effect of such inclusions on the degradation rate of FeMn-based alloys has not yet been investigated, however Hermawan et al. [19] suggested their potential at triggering micro-galvanic corrosion by providing microsites with different potential than the base metal. Besides these aspects, elemental segregation at grain, or particle boundaries, has been shown to have positive effects on corrosion acceleration for both powder-processed Fe30Mn microstructures [39] as well as induction melted Fe30Mn1C [18]. Similarly, tuning the grain sizes also has a marked effect on the degradation rate of both powder-processed [29] and wrought [40] Fe-based materials.

In a simplified way, the typical degradation reactions of Fe can be presented as follows:

$$Anodic\ reaction : Fe \rightarrow Fe^{2+} + 2e^- \tag{1}$$

$$Cathodic\ oxygen\ reduction\ reaction, (ORR) : O_2 + 4e^- + 2H_2O \rightarrow 4OH^- \tag{2}$$

$$Hydrolysis\ reactions : Fe^{2+} + 2H_2O \rightarrow Fe(OH)_2 + 2H^+ \tag{3}$$

$$Fe^{3+} + 3H_2O \rightarrow Fe(OH)_3 + 3H^+ \tag{4}$$

$$Oxidation\ reaction : 4Fe(OH)_2 + O_2 + 2H_2O \rightarrow 4Fe(OH)_3 \tag{5}$$

The corrosion of pure Fe is accompanied by alkalinisation owing to the ORR, controlled by the diffusion of dissolved oxygen from the electrolyte to the metal interface. The hydrolysis of Fe^{2+} and Fe^{3+} leads to acidification in the anodic sites of metal dissolution [7,41]. However, in practice, the corrosion of pure Fe in both *in vivo* and *in vitro* environments are more complicated due to the involvement of multiple organic/inorganic components, which not only buffer the pH value but also induce the formation of complex compounds that complicate the corrosion behaviour. Consequently, studying the correlation between pH variation and media compositions has become a very important aspect in the field of biodegradable metals.

Even though the pH variation during metal degradation has received gaining concerns from researchers [16,42], the main focus is typically on the overall pH variation of the bulk electrolyte rather than the evolution of local pH. The latter is predetermined by the rate of the anodic and cathodic reactions, accompanied hydrolysis reactions and composition of precipitates. The local pH also controls the secondary reactions at the metal interface and factually provides precise information for further comprehension of the corrosion behaviour. Therefore, understanding the origin and the evolution of the local pH at the interface of corroding alloys is highly relevant for unravelling complex degradation mechanisms. Local pH measurements are typically conducted in potentiometric mode of localized techniques e.g. Scanning Electrochemical Microscopy (SECM) [43] and Scanning Ion-selective Electrode Technique (SIET) [44], which are regarded as powerful tools to detect various ion concentrations and follow the development of local ion concentration via continuously imaging its distribution. For instance, detecting ion concentrations has been employed for biological applications for decades [45–47]. Recently, Lamaka et al. [48] and Mei et al. [49] have reported local pH and its evolution near the surface of Mg alloys exposed to various SBFs, providing strong evidence for lower degree of alkalinisation during corrosion of Mg alloys compared to that

commonly believed based on previous knowledge about local pH of Mg dissolution in an aqueous electrolyte solely composed of NaCl. Moreover, Tris-HCl and HEPES buffers have been found to be unable to stabilize the local pH of Mg in SBF [48,50]. Such *in vitro* studies on biodegradable Mg alloys have paved the path for in-depth investigations on biodegradable Fe-based alloys. Besides, it is equally worth investigating the evolution of local concentration of dissolved oxygen [51–53], which plays an essential role during Fe corrosion and normal biological function [54]. However, there is a lack of direct *in situ* studies exploring the evolution of oxygen concentration during corrosion of Fe and its alloys. Recently, the state-of-art *in situ* technique that maps local pH together with dissolved oxygen (DO) concentration has been applied in corrosion studies [55–57]. Using the combination of these two advanced localized techniques, unravelling the mechanisms behind the corrosion of Fe and its alloys becomes possible. This gives researchers the opportunity to break new ground in the emerging field of biodegradable Fe and its alloys.

In this work, the evolution of local pH and DO concentration of three Fe-based alloys; pure Fe, Fe35Mn and (Fe35Mn)5Ag, was systematically investigated via *in situ* simultaneous monitoring of local pH and DO concentration in HBSS at 37 °C under hydrodynamic condition. The use of HBSS with and without Ca^{2+} ions, was adopted in this study based on previous results in order to highlight the importance of Ca^{2+} ions during degradation of biodegradable metals. This study aims at providing *in situ* experimental evidence during the degradation of Fe, Fe35Mn, (Fe35Mn)5Ag biodegradable alloys. This evidence can be used to hypothesise about degradation mechanisms and also understand the role of the alloying elements and medium components during *in vitro* biodegradation of these iron-based alloys.

2. Materials and methods

The Fe, Fe35Mn (hereafter FeMn) and (Fe35Mn)5Ag (hereafter FeMnAg) samples used in this work were prepared by mixing individual powders which were uniaxially pressed and sintered. Raw powders: Fe (particle size <45 μm, 99% purity, US Research Nanomaterials Inc. USA), Mn (particle size <10 μm, 99.6% purity, Alfa Aesar, Germany) and Ag (particle size 4–7 μm, 99.9% purity, Alfa Aesar, Germany) were mixed in the ratio specified above in a Bio-Components Inversina tumbler (Switzerland) for 5 h with stainless steel balls. In the case of (Fe35Mn)5Ag, the amounts of Fe and Mn were adjusted to have a 65:35 Fe to Mn ratio. The use of 5 wt% Ag in this alloy, as opposed to lower concentrations, is aimed at amplifying any effects Ag may have on the degradation behaviour of FeMnAg. A 6 g powder charge was uni-axially pressed in an 8 mm diameter die at a pressure of 1.8 GPa using an Instron 8802 hydraulic press (USA) in order to create cylindrical green compacts. These green compacts were then introduced into a Nabertherm tube furnace (Germany) having a 100 L/h of N_2–$5H_2$ flow, were heated at a rate of 180 °C/h, sintered at 1120 °C for 3 h and allowed to cool to room temperature inside the tube furnace. Fig. 1 shows the microstructure of samples used in this study. The reasons behind the differing density of Fe compared to the FeMn-alloys of interest, has been provided in Part I of this work [58] along with further details on material characterization. The coupons were then machined to obtain a final diameter

of 3 mm. Samples were embedded in epoxy resin (Buehler, EpoxiCure™, USA), ground and finally polished using colloidal silica of approximately 0.04 μm (Struers, Denmark). All samples were ultrasonically cleaned in ethanol before commencing with local measurements.

The spatially resolved experiments were carried out at 37 °C in simple HBSS (ThermoFisher Scientific, no. 14175095) hereafter referred to as HBSS, and modified HBSS (ThermoFisher Scientific, no. 14025100), hereafter referred to as HBSS + Ca. The latter consisted of the HBSS formulation with additional $CaCl_2$, $MgCl_2 \cdot 6H_2O$ and $MgSO_4 \cdot 7H_2O$ (see Table 1).

To monitor the DO concentration, a needle-type retractable fiber-optic oxygen micro-optode with a tip diameter of 50 μm coupled with FireStingO₂ oxygen logging meter, both from Pyroscience™ (Germany) was used. Local pH was measured by a glass-type pH microelectrode from Unisense (Denmark) with a tip length of 50 μm and tip diameter of 10 μm. A Ag/AgCl electrode was adapted as an external reference electrode. Both DO micro-optode and pH micro-electrode were integrated in a commercial SVET-SIET system from Applicable Electronics™ (USA) for probes movement. The data is acquired by LV4 software from Scienceware™ in parallel with PyroOxygenLogger from Pyroscience™. The pH microelectrode and DO micro-optode were positioned at 50 μm above the sample surface. The distance between the pH microelectrode and DO micro-optode was controlled using micromanipulators and kept at 50 μm in horizontal plane using a custom-made dual-head stage micromanipulator, allowing for *in situ* simultaneous monitoring of the evolution of pH and DO concentration [55]. A schematic of the test setup can be seen in Fig. 2.

For the distribution of local pH and DO concentration on the specimen surface, initially, a general sample-centred area (4000 μm × 4000 μm) was scanned with the rate of 200 μm per step in order to quickly obtain an integral distribution. Subsequently, a representative area (2000 μm × 4000 μm) was selected and scanned with the rate of 80 μm per step to follow the local progression over 24 h. The sampling interval was 3 s and the total time for one map (25 × 50 grid) was approximately 1.5 h including the time needed to move the micro-sensors (30 min for the first map). The optical images displayed were taken at the end of each mapping. For line-scan measurement, the step length was 50 μm and the sampling interval was 5 s leading to a total time of around 15 min for one 200-point line. All the measurements were conducted at 37 °C under hydrodynamic conditions with a flow rate of 1.0 mL/min.

Table 1
The formulation of HBSS and HBSS + Ca electrolytes used in this study.

Components	HBSS (mM)	HBSS + Ca (mM)
KCl	5.333	5.333
KH_2PO_4	0.441	0.441
$NaHCO_3$	4.167	4.167
NaCl	137.9	137.9
Na_2HPO_4	0.338	0.338
$CaCl_2$	–	1.261
$MgCl_2 \cdot 6H_2O$	–	0.493
$MgSO_4 \cdot 7H_2O$	–	0.407
D-Glucose	5.556	5.556
pH $_{initial}$	7.2–7.4	
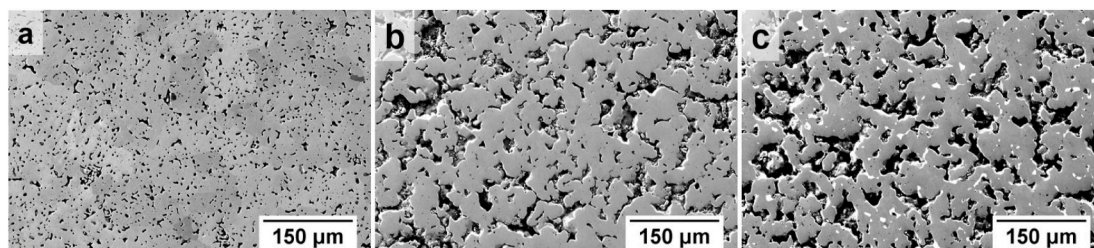
Fig. 1. SEM images of the ground and polished samples. (a) Fe, (b) FeMn and (c) FeMnAg.
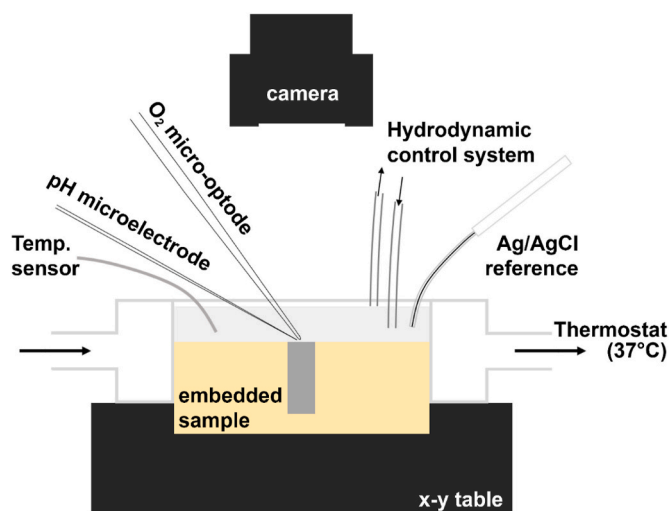
Fig. 2. The schematic setup for simultaneous measurements of local pH and dissolved oxygen concentration.

3. Results

3.1. Local pH and DO concentration of Fe-based alloys in HBSS

Fig. 3 shows the visual appearance and the distribution of local pH and DO concentration of Fe-based alloys immersed in HBSS from 20 to 60 min. Different accumulations of corrosion products were evident on the surface of these alloys as indicated in their optical images, and distinguished acidification and alkalization regions were displayed on the local pH distribution map which shows the balanced effect of active anodic and cathodic reactions. The integrated information of the visual appearance and the distribution of local pH indicated that localized corrosion occurred on the sample surface within the first hour of immersion in HBSS. Meanwhile, DO consumption, which is predominantly related to the cathodic oxygen reduction reaction, was observed with gradients due to oxygen diffusion in the electrolyte. The relatively higher oxygen consumption on the left surface area of pure Fe corresponds to formation of bright precipitates of corrosion products.

By contrast, visually more severe corrosion rapidly progressed over the surface area of FeMnAg sample than Fe and FeMn. A wide range of pH variation, with lowest pH (6.40) and highest pH (8.10), was detected in anodic and cathodic sites respectively. In the corresponding DO map, approximately 0.50 mg/L of DO concentration was recorded on massive areas. In order to better monitor the rapid evolution of localized behaviour, quick line scans were sequentially executed across the FeMnAg sample surface (Fig. 4). Evidently, distinct acidification and alkalization sites on the surface of FeMnAg were reflected on pH line scans correlating with the corrosion appearance in the optical images. With increasing immersion time, both acidification and alkalization progressively weakened due to the considerable coverage of corrosion products, which concurrently blocked the oxygen diffusion and the intensive oxygen consumption gradually decreased (Fig. 4). Yet, the concentration of O_2 remained rather low, 0.75–1.2 mg/L. This is considerably lower than O_2 concentration in naturally aerated HBSS which is measured at 5.8 $\pm$ 0.2 mg/L at 37 °C. After 15 h from immersion, the severe accumulation of corrosion products on the surface of FeMnAg started to interfere with the operation of the pH microelectrode and oxygen micro-optode, which were positioned only 50 μm above the sample surface. In order to prevent sensor damage and unreliable measurements while also maintaining a uniform positioning of the probes with respect to the sample surface, this measurement was stopped at the 15-h mark.

Given that the initial local pH and DO measurements presented in **Part I** of this work, as well as the changes observed on the

microstructure during the experiment, indicated less drastic changes in the local environment over the initial 15 min from immersion (see the initial local results in **Part I** of this work [58], which are also consistent with previous reports [29]), mapping was suitable to follow the evolution of local pH and DO concentration above their surfaces. A representative area was selected to reflect the distribution of local pH and DO concentration (Fig. 5). As seen in the optical images of pure Fe, there were generated bright corrosion products which turned dark starting on the left surface area, where the oxygen consumption was enhanced: the value of DO concentration (1.90–3.00) was lower than that (2.40–4.10) in Fig. 3. The darkening of corrosion products on the surface of pure Fe proceeded until 24 h with a further decrease of DO concentration (1.55–2.05) compared to that (1.90–3.00) by 12 h. On the other hand, both the accumulation of corrosion products and the distribution of local pH was observed to be uniform on Fe and FeMn, where the initial localized corrosion evolved into general corrosion. Slightly higher pH minimum for FeMn (7.20–7.23) compared to that of pure Fe (7.07–7.09) signifies that hydrolysis of dissolved iron species was slightly inhibited during degradation of FeMn in HBSS. The minimum value of DO concentrations continued decreasing from 12 h to 24 h (2.38–1.78), accompany by slight increase of local pH values (7.23–7.28 to 7.20–7.32).

3.2. Local pH and DO concentration of Fe-based alloys in HBSS + Ca

The visual appearance and distribution of local pH and DO concentration of Fe-based alloys in HBSS + Ca are shown in Fig. 6. From the distribution of local pH, similar localized corrosion took place on the surface of Fe-based alloys in HBSS + Ca, compared to that in Fig. 3. Compared with the pH ranges of Fe (6.76–7.36), FeMn (7.20–7.39), and FeMnAg (6.49–8.10) in HBSS (Fig. 3), weaker acidification and alkalization related to a narrower pH range (7.05–7.30 for Fe; 7.16–7.30 for FeMn; 7.10–7.80 for FeMnAg) were detected in HBSS + Ca at the initial stages. The minimum DO concentration for FeMn was 4.15 mg/L i.e. twice as high as that in HBSS (2.04 mg/L). Although FeMnAg still possessed the largest pH range (7.10–7.80) compared to that of pure Fe (7.05–7.30) and FeMn (7.16–7.30), a significant difference was found on FeMnAg between its immersion in HBSS and HBSS + Ca. The FeMnAg sample exhibited lower corrosion activity in HBSS + Ca (Fig. 6) than that in HBSS (Fig. 3). This follows from comparison of the optical images, a narrower pH range: 7.10–7.80 (vs. 6.49–8.10 in HBSS) and lower DO consumption: 4.90–5.65 (vs. 0.50–1.40 in HBSS), indicating that both anodic and cathodic reactions on FeMnAg were considerably inhibited in HBSS + Ca.

Considering that contrasting corrosion behaviour occurred on the surface of FeMnAg, the particular evolution of the visual appearance and the distribution of local pH and DO concentration of FeMnAg is presented in Fig. 7. The visual appearances were well-correlated to the distribution of local pH during 24 h of immersion. The sites of highest and lowest local pH shifted within the first 6 h of immersion. When overlaying the optical image over the local pH plot, it is apparent that the corrosion products mostly generated at the location of initial anodic site, and after 6 h, fresh corrosive spots appeared precisely related to the new anodic sites, as indicated in Fig. 7. Meanwhile, barely any differences were shown in the distribution of DO concentration, meaning that the corrosion progressed slowly. At the 12-h mark, the anodic site established after 6 h remained active and started to grow broader associated with an obviously growing consumption of dissolved oxygen: the minimum of DO concentration reduced twofold from approximately 5.00 mg/L to 2.50 mg/L. Afterwards, the regions of lower pH continued enlarging until 24 h, while the pH minimum stabilized at around 7.1. Meanwhile, DO consumption further intensified (the minimum of DO concentration decreased down to 0.40 mg/L) while an accumulation of dark corrosion products in the optical image was also evident. Remarkably, in spite of the intensive oxygen consumption accompanied by generation of hydroxyl ions, local pH did not rise above 7.3 after one
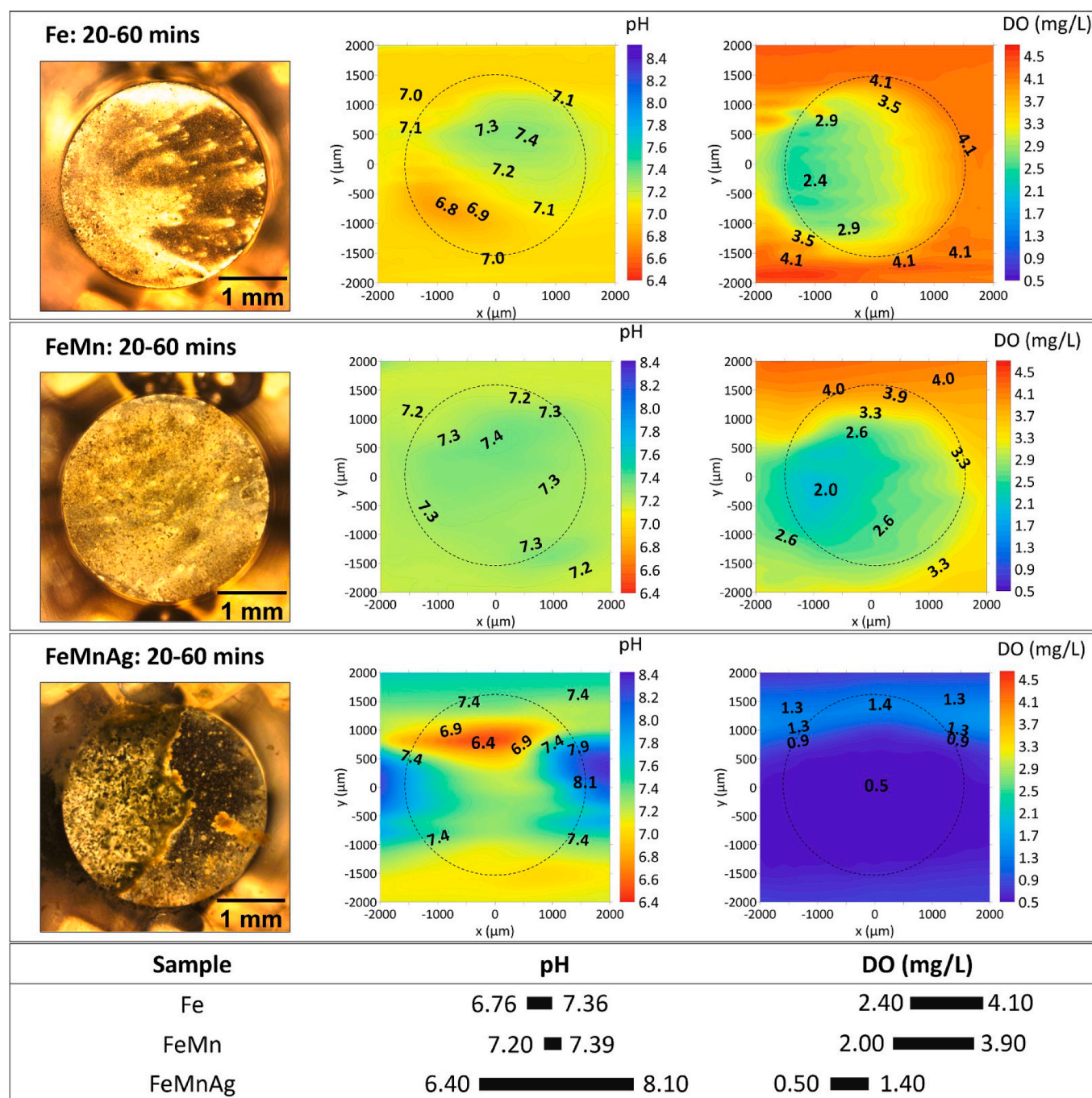
Fig. 3. The visual appearance, distribution of local pH and DO concertation above Fe, FeMn and FeMnAg samples after 20–60 min of immersion in HBSS. The section below summarizes the variation ranges of pH and DO.

day of immersion. This clearly indicates fast consumption of hydroxyl ions for formation of precipitated corrosion products that buffered further increase of local pH.

In the case of pure Fe (Fig. 8), rapidly formed bright products in the optical image covered the majority of pure Fe surface within 1 h. The coverage continued extending over the whole surface and the corrosion products proceeded to grow until 24 h. Meanwhile, local pH gradually became more uniform, demonstrating that the initial localized corrosion evolved into general corrosion with immersion time. The pH maximum was relatively stable, but the pH minimum gradually increased from 7.03 (1 h) to 7.22 (24 h), implying lower availability of Fe ions that are the typical cause of lower pH due to hydrolysis. On the other hand, decrease of DO concentration (down to 0.45 mg/L) indicates that the

products layer was not able to hinder the diffusion of DO from electrolyte to Fe surface. Likewise, similar uniform degradation behaviour was found on FeMn (Fig. 9). Compared to the slowly increased minimum of local pH above pure Fe, the pH minimum above FeMn was maintained at around 7.10 until 24 h while the pH maximum slowly rose from 7.23 to 7.32, associating with the decreasing minimum of DO concentration (from 3.15 to 1.90 mg/L). Just like in the case of FeMnAg, considering the pH range of Fe and FeMn were rather stable, the significant DO consumption probably contributed to further oxidation of Fe corrosion products.
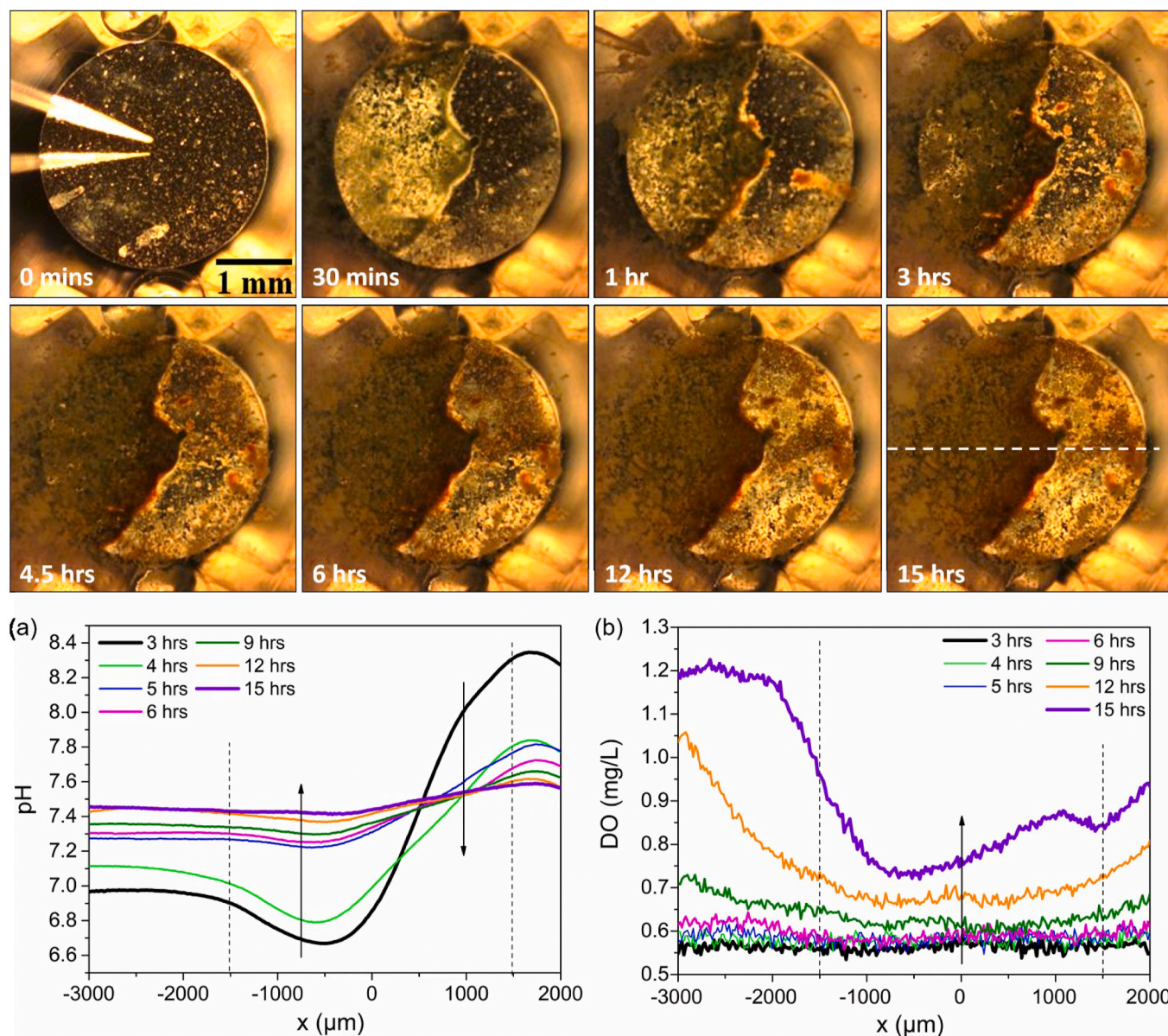
Fig. 4. The visual appearance of FeMnAg in HBSS after specified immersion time and the line-scans (a) local pH and (b) DO concentration across the sample surface. White dashed line shows the position of the line-scans. Black dashed lines indicate sample position. The pH and O_2 micro-probes positioned for the measurements are seen in the first optical micrographs.

4. Discussion

4.1. The influence of the alloying elements (Mn, Ag) on the biodegradation of Fe-based alloys in HBSS

Based on the results presented in section 3.1, varying degradation behaviour was revealed for pure Fe, FeMn and FeMnAg in HBSS, respectively. In a simple saline solution, it is relatively simple to directly evaluate the influence of the pH change on the degradation behaviour. However, in a complex medium like HBSS, various degradation products form in different pH ranges. The influence of the change of local pH on the degradation behaviour, is highly relevant to the dissolution-precipitation of these degradation products. It is these complex degradation products that have a significant influence on the degradation behaviour of the alloy. Local pH thus acts as an important factor in differentiating between degradation phenomena by indicating the formation of possible products that control the degradation behaviour. The samples used in this work were porous powder metallurgy alloys

(Fig. 1), and hence it is difficult to judge the corrosion type by a microscopic magnification on an area of interest since anodic dissolution could also progress in micro-cavities. The influence of micro-cavities on these samples could not be eliminated during experiment. These micro-cavities form an integral part of the corrosion and its mechanisms of materials produced by powder metallurgy. On the other hand observation of local pH and DO gives useful information on the corrosion progression despite the presence of the micro-cavities.

With the information provided by the distribution of local pH, typical localized corrosion was characterized on the surface of pure Fe (Fig. 3): anodic and cathodic sites could be associated with slightly more acidic and alkaline local pH due to reactions (Eqs. (1)–(4)). The hydrolysis of Fe^{2+} and Fe^{3+} cations (Eqs. (3) and (4)) that leads to local acidification, was overpowered in the presence of HPO_4^{2-} and HCO_3^-, preventing higher H^+ concentrations from being reached, as shown in Fig. 10, justifying only moderate acidification on the surface of pure Fe in HBSS. On the other hand, dissolved oxygen (DO) was consumed over the whole sample (Fig. 5), due to cathodic oxygen reduction reaction (ORR) and
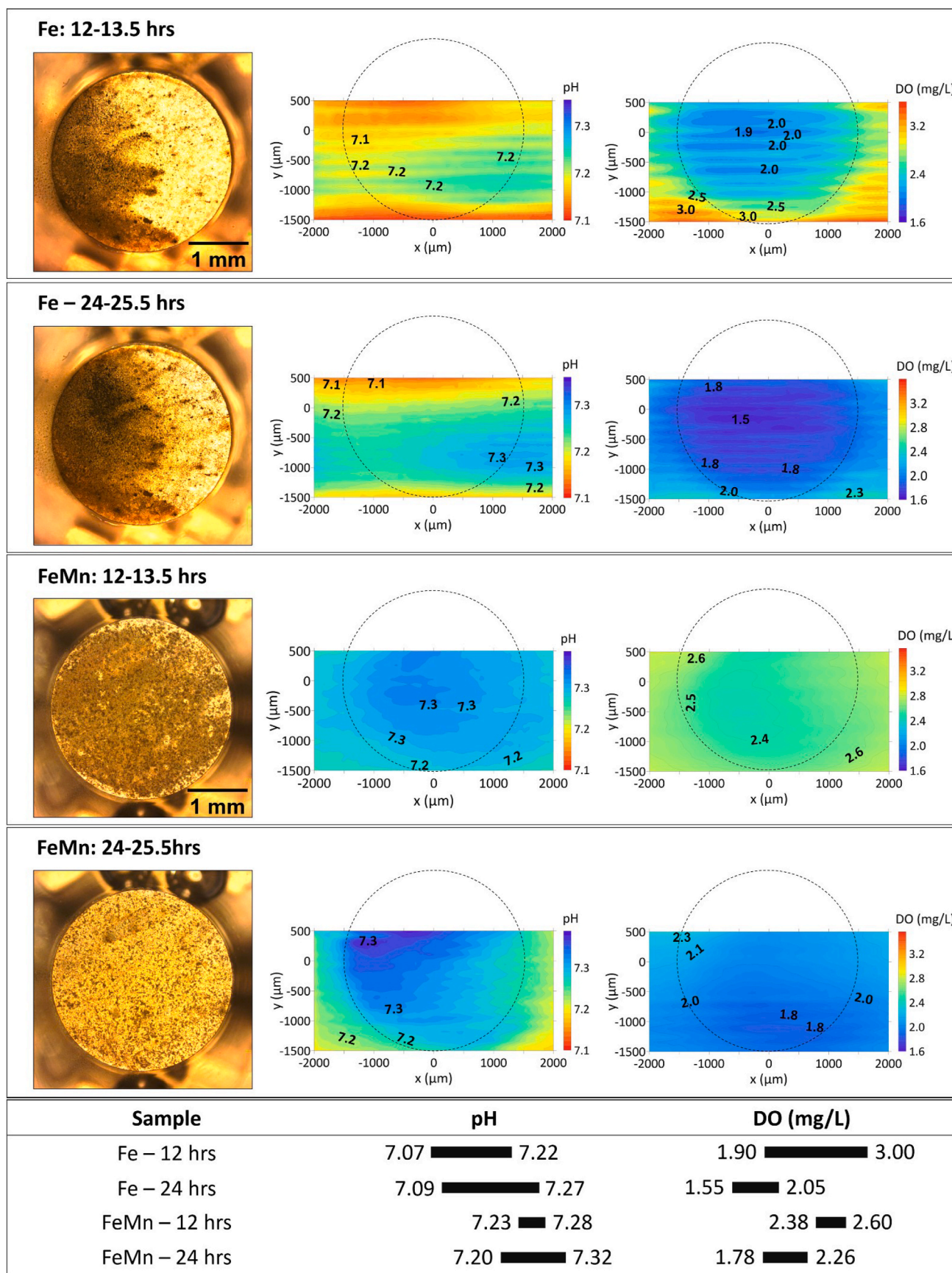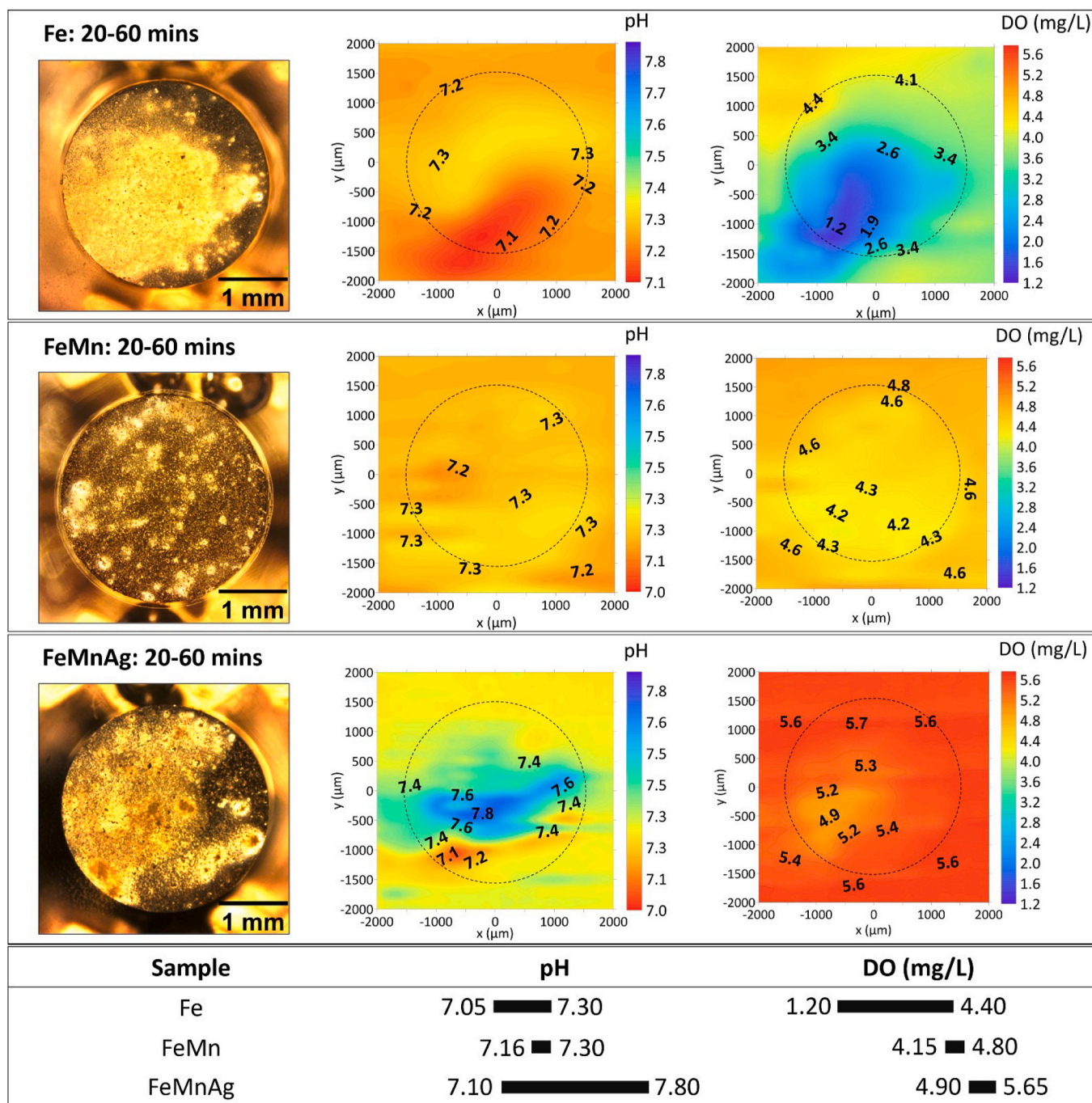
Fig. 5. The visual appearance, distribution of local pH and DO concertation for Fe and FeMn after 12 and 24 h of immersion in HBSS. The section below summarizes the variation ranges of pH and DO.

Fig. 6. The visual appearance, distribution of local pH and DO concertation for Fe, FeMn and FeMnAg after 20 min immersion in HBSS + Ca. The section below summarizes the variation ranges of pH and DO.

oxidation of ferrous (Fe^{2+}) products to form more stable ferric (Fe^{3+}) compounds (Eq. (5)).

Local compositional inhomogeneities of FeMn and the presence of MnO inclusions on the surface, as described in Part I of this work [58], could have led to formation of micro-galvanic couples, resulting in a stronger cathodic response on FeMn than that on Fe, as seen in the initial local pH/DO monitoring in Part I of this work [58]. In addition, the preferential formation of Mn-phosphates among corrosion products, as shown in the SEM/EDS analysis and MEDUSA calculations [59] in Part I of this work [58], did not inhibit the unceasing substrate dissolution and the persistent oxygen consumption that proceeded in the next 24 h (Fig. 5). Therefore, in this case, Fe35Mn degraded faster than pure Fe (according to the corrosion currents in Part I of this work [58]), and the

accumulated Fe- and Mn-phosphate products on the surface barely have any protective effect.

Ag addition had a significant influence on the degradation behaviour of the Fe–Mn alloys. The uniformly distributed Ag phase served as active cathodic sites even in the presence of similar Mn-phosphates deposits, activating strong anodic and cathodic reactions and fast electron and mass transport, thus promoting the dissolution of both Fe and Mn. The hydrolysis of increasingly dissolving Fe ions produced more H^+ ions than that on Fe and FeMn, causing an enhanced acidification at active anodic sites within the first 3–4 h immersion (as indicated by the low pH (6.7–6.9) in Fig. 4). The high pH of 8.4 at cathodic sites indicated a stronger cathodic reaction occurring on FeMnAg when compared to Fe and FeMn. With time, local pH at anodic sites increased from 6.7 to 7.4
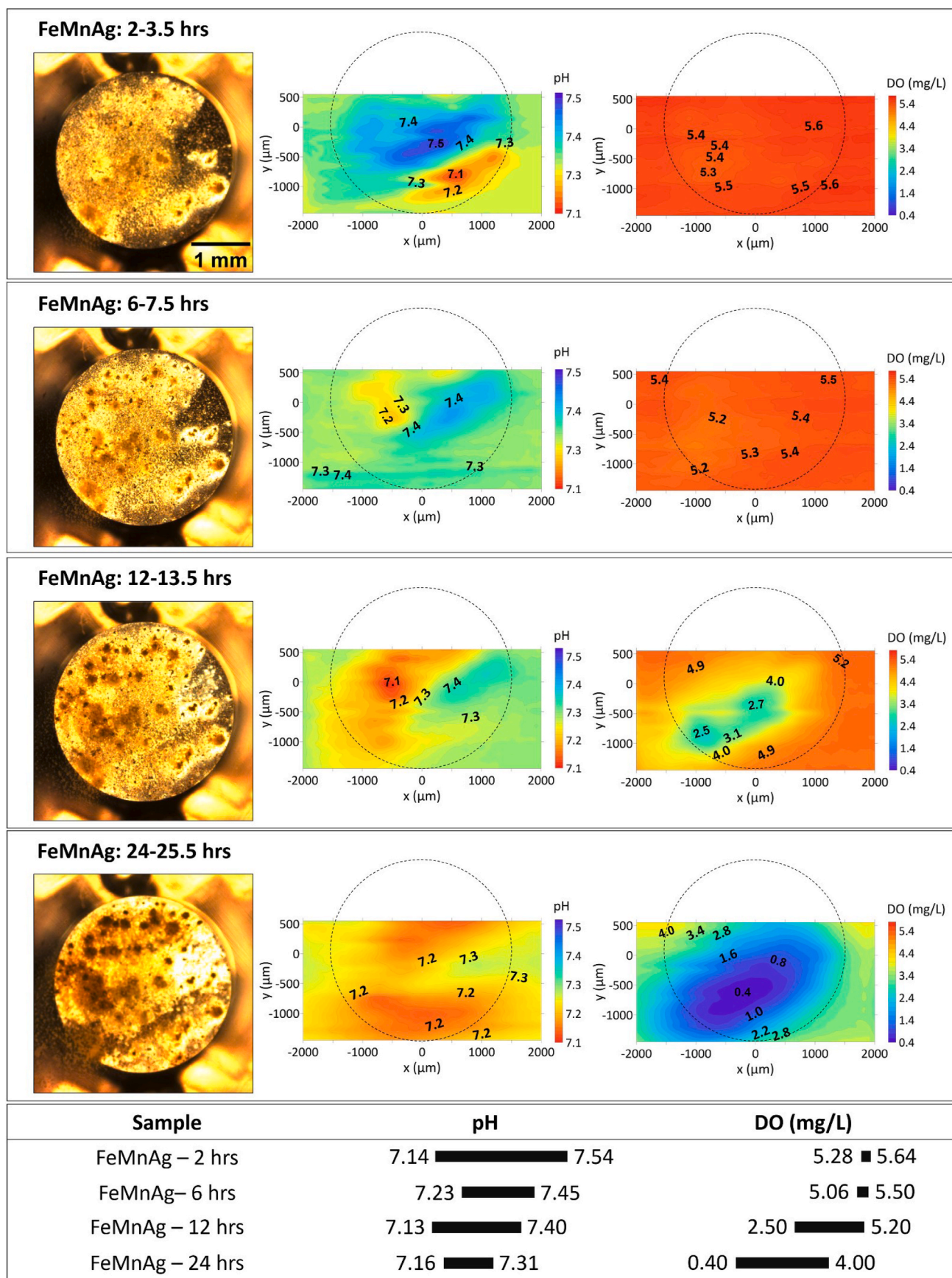
Fig. 7. The visual appearance, distribution of local pH and DO concentration for FeMnAg after 2–24 h immersion in HBSS + Ca. The section below summarizes the variation ranges of pH and DO.
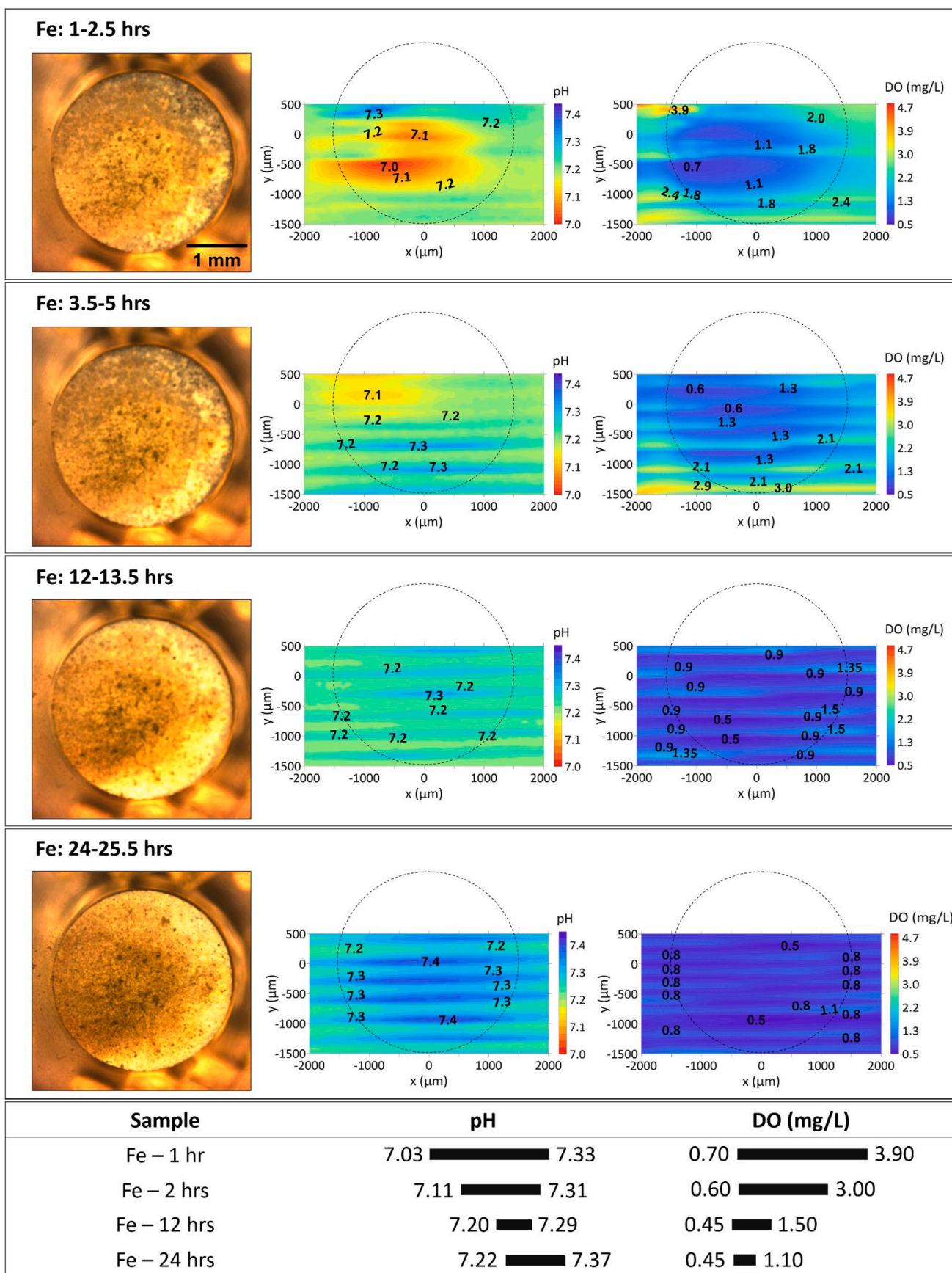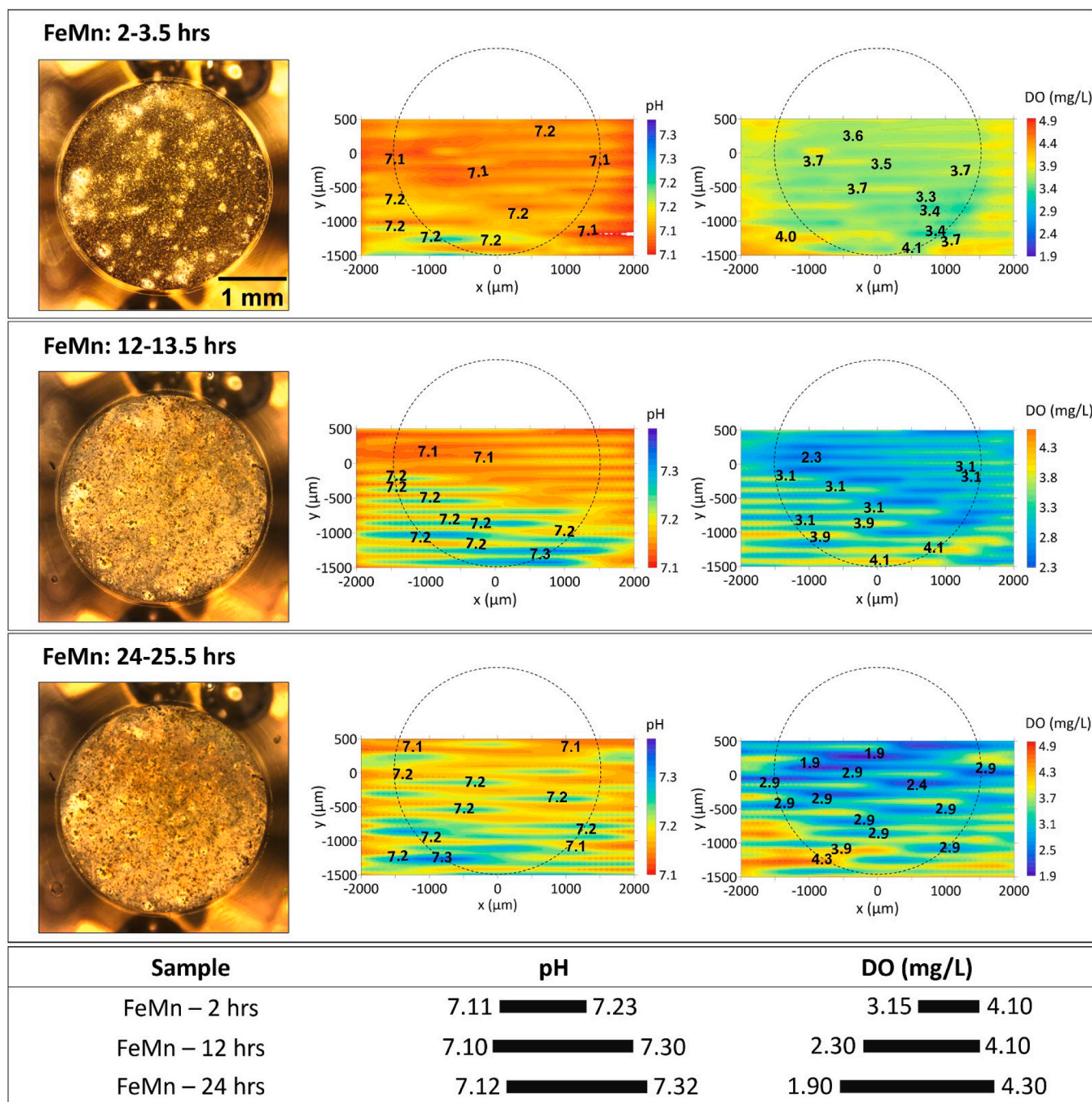
Fig. 8. The visual appearance, distribution of local pH and DO concentration for Fe after 1–24 h immersion in HBSS + Ca. The section below summarizes the variation ranges of pH and DO.

Fig. 9. The visual appearance, distribution of local pH and DO concertation for FeMn after different immersion time in HBSS + Ca. The section below summarizes the variation ranges of pH and DO.

(bulk pH), indicating a decreasing amount of hydrolysed Fe ions due to the formation of Fe-containing corrosion products. The rate of strong electrochemical reaction reached the limit controlled by the diffusion of dissolved oxygen. Meanwhile, SEM/EDS analysis in Part I of this work [58] indicated that Ag remained exposed after 24 h, which provided persistent sites for the cathodic reaction, supporting anodic dissolution of the less noble austenitic matrix. The corrosion products above Ag particles were not dense enough to block dissolved oxygen from reaching the surface where the ORR (Eq. (2)) took place. It is also useful to note that the higher surface area of FeMnAg compared to the Fe alloy, due to increased percentage porosity, could have contributed to the higher anodic dissolution and localized corrosion observed on the alloy. On the other hand, although FeMn had a similar percentage porosity to

FeMnAg, this did not seem to impact the degradation of FeMn in the same way.

4.2. The influence of Ca^{2+} ions in HBSS on the biodegradation of Fe-based alloys

In general, the presence of Ca^{2+} ions in HBSS electrolyte reduced the degradation rate of pure Fe, FeMn and FeMnAg, as seen in the corrosion currents present in Part I of this work [58]. Ca^{2+} ions were able to combine with PO_4^{3-} and OH^- generated by ORR to precipitate Ca–P-containing products on the metal surface. The precipitation of Ca–P-containing products layer not only resulted in decreasing OH^- levels reflected by the lower local pH compared to that in the absence of
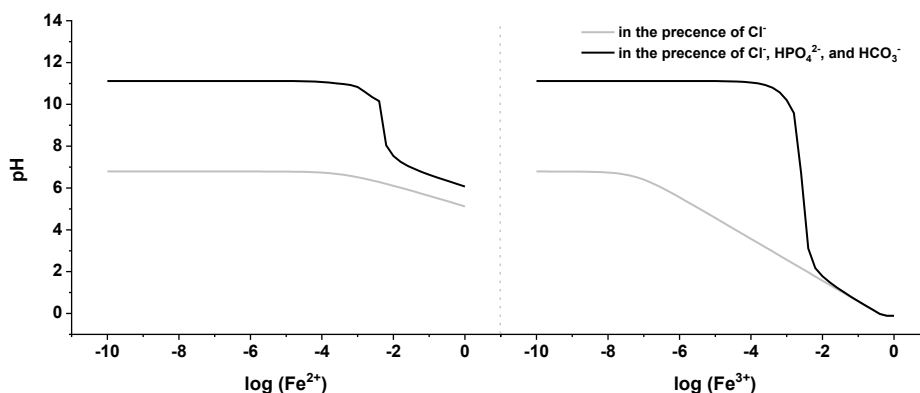
Fig. 10. pH value caused by the hydrolysis of varying concentration of Fe^{2+} and Fe^{3+} in presence of 143.26 mM Cl^-, or that with 0.78 mM HPO_4^{2-} and 4.17 mM HCO_3^- [48].

Ca^{2+} ions, but also acted as a partially protective layer that impeded the diffusion of dissolved oxygen from electrolyte to the metal surface, thus slowing down the ORR at cathodic sites (Fig. 6).

Despite the similar visual appearance and distribution of local pH and DO concentration featured on pure Fe in Figs. 3 and 6, the corrosion current of Fe (presented in Part I of this work [58]), further decreased in the presence of Ca^{2+} ions due to the formation of Ca–P-containing products layer on the metal surface. The continuous coverage and barrier properties of this layer were manifested by growing time constant at high frequencies identified in Bode plots of EIS spectra in Part I of this work [58]. Sluggish degradation of pure Fe produced a limited amount of OH^-, causing the coverage of Ca–P precipitates to slowly progress on the surface. Meanwhile, the consumption of PO_4^{3-} by Ca^{2+} ions hindered the formation of Fe-phosphates, probably leading to an alternative growth of Fe-carbonates (as seen in the Medusa diagram in Part I of this work [58]). The darker products in the optical images in Fig. 8, could also be an indication that the consumption of DO was related to the formation of ferrous corrosion products forming outside pitting sites [5, 16], which was also supported by the SEM images presented in Part I of this work [58]. Compared to pure Fe, slight quantitative variations on the distribution of local pH and stable DO concentration were characterized on FeMn (Figs. 5 and 9). After 24 h, the DO range in HBSS + Ca (1.90–4.30 mg/L) was larger than that in HBSS (1.78–2.26 mg/L), indicating lower DO consumption above the surface of FeMn in HBSS + Ca compared to that in HBSS.

At the initial stage of FeMnAg degradation, calcium phosphates were easier to precipitate on the surface than on Fe and FeMn, especially on Ag particles where ORR quickly provided quantities of OH^- sufficient for the formation of Ca–P-containing products, as seen in initial local measurements presented Part I of this work [58]. The precipitation of Ca–P-containing products accounted for the lower local pH (max. 7.8) above the surface of FeMnAg in HBSS + Ca than that in HBSS (max. 8.4), and in turn blocked the oxygen diffusion, leading to such a sluggish ORR at cathodic sites that significantly weakened the initially strong cathodic activity (Fig. 6 and the initial local measurements in Part I of this work [58]). The reduced cathodic activity inhibited the anodic dissolution of the Fe-based substrate. The amount of hydrolysed Fe ions decreased, so local pH at anodic sites of degrading FeMnAg in HBSS + Ca was higher (min. 7.1) at the initial stage than that in HBSS (min. 6.7). However, it could be speculated that formed protective corrosion products, partially detached from the surface or changed their structure during continuous degradation, resulting in more pathways for DO diffusion (Fig. 7). This assumption is supported by EIS results presented in Part I of this work [58], where the resistance associated with the formed Ca–P-containing products layer decreased after around 9 h, with a corresponding shift in corrosion product layer capacitance, both indicating a decreasing impedance contribution from the protective layer. Even so, compared with the results of FeMnAg in HBSS (Fig. 4) at the same timeframe (after

12–15 h of immersion), DO was consumed less on the surface of FeMnAg in HBSS + Ca (min. 2.5 mg/L) than that in HBSS (min. 0.7 mg/L). DO was also consumed outside the active pits for oxidation of ferrous products to ferric species as evidenced by progressive formation of darker products, accounting for the minimum value of DO concentration decreasing to 0.41 mg/L and the area of DO consumption becoming extensively large from 12 h to 24 h (Fig. 7). XRD was attempted to characterize the corrosion products. However, due to the limited amount of the corrosion products and porous structure of the sample, the signal from the corrosion products was overshadowed by the characteristic peaks of the Fe, FeMn, Ag and MnO phases in the substrate. Besides, some amorphous corrosion products may not be identified by XRD. In future work, other surface characterization techniques such as XPS will be considered to obtain more information about the specific corrosion products formed on these samples.

In summary, as Ca^{2+} ion is an indispensable inorganic component in the physiological fluid and always present in orthopaedic implantation sites, understanding correlation between degradation and formation of Ca–P-containing products is of crucial importance. This study has indicated that such products formed within the first few minutes upon exposure to the Ca^{2+}-containing electrolyte. It is worth mentioning that although local pH maintained generally neutral at the metal interface, the proceeding high rate oxygen consumption resulted in an intensely low concentration of O_2 remaining in the electrolyte adjacent to the degrading metal (as summarized in Fig. 11). Thus, it is reasonable to speculate that biodegradable Fe-based implants could potentially lead to hypoxemia around the implantation sites, where blood oxygen could be excessively consumed. Moreover, *in vivo* hydrogen evolution has been reported in Fe–35Mn–1Ag currently [60]. Based on our findings, it could be possible to trigger hydrogen evolution around the Fe-based implants, as water may start being reduced to hydrogen gas when there is hardly any blood oxygen.

5. Conclusions

The evolution of local pH and O_2 concentration during degradation were simultaneously monitored at the interface of pure Fe, FeMn and FeMnAg in HBSS and HBSS + Ca electrolytes assisted by advanced localized techniques.

The main conclusions are the following:

For pure Fe and FeMn, localized corrosion behaviour dominated at the beginning of immersion. At the later immersion stage, after 12–24 h, the corrosion process progressed uniformly. The addition of 5 wt% Ag to the FeMn alloy created effective micro-galvanic couples between austenitic FeMn matrix and Ag, which served as efficient cathodic sites for oxygen reduction reaction (ORR).

In HBSS + Ca electrolyte, the local pH values above three alloys remained in a narrower range (7.03–7.80) than that in HBSS
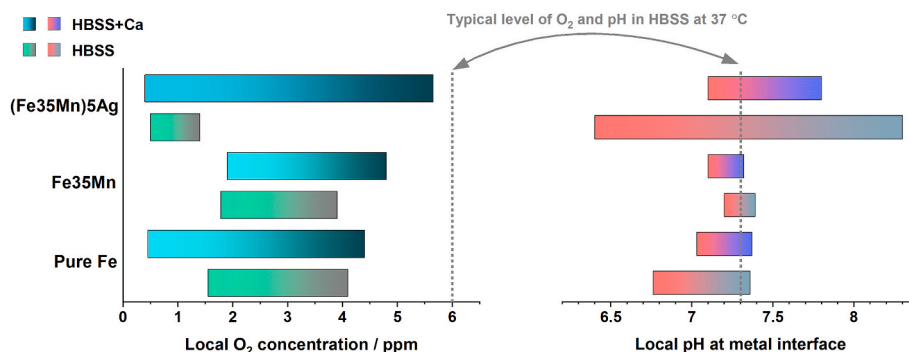
Fig. 11. The summarized range of local pH and O_2 concentration at the interface of pure Fe, FeMn, and FeMnAg during 24 h of immersion in HBSS and HBSS + Ca (For FeMnAg in HBSS, the immersion time was up to 15 h).

(6.40–8.30). This is attributed to the precipitation of Ca–P-containing products on the metal surface that stabilizes the local pH, particularly for FeMnAg. Cathodic ORR on Ag-rich sites produced quantities of OH^-, favouring deposition of Ca–P-containing products. As immersion time elapsed, Ca–P-containing products detached from FeMnAg surface, exposing the degrading material underneath to interact with the dissolved oxygen, while Fe and FeMn degraded uniformly with less coverage of Ca–P-containing products on the surface than FeMnAg.

Notably, DO concentrations above all three alloys proceeded decreasing during 24 h. In spite of this active oxygen consumption, interface pH largely remained neutral. This indicates O_2 consumption for oxidation of Fe^{2+} to Fe^{3+} and intake of generated OH^- for hydroxide and phosphate precipitation. Furthermore, local concentration of remaining oxygen decreased to 0.5 mg/L from 6 mg/L characteristic for naturally aerated HBSS. This suggests that low oxygen concentration can affect the physiological environment of the implantation site.

CRediT authorship contribution statement

Cheng Wang: Data curation, Visualization, Formal analysis, Investigation, Writing – original draft, Writing – review & editing. **Christabelle Tonna:** Data curation, Visualization, Formal analysis, Investigation, Writing – original draft, Writing – review & editing. **Di Mei:** Investigation, Writing – review & editing. **Joseph Buhagiar:** Conceptualization, Supervision, Writing – review & editing. **Mikhail L. Zheludkevich:** Conceptualization, Supervision, Writing – review & editing. **Sviatlana V. Lamaka:** Conceptualization, Supervision, Writing – review & editing.

Declaration of competing interest

The authors declare that they have no competing interests.

Acknowledgements

References

[1] M. Peuster, C. Hesse, T. Schloo, C. Fink, P. Beerbaum, C. von Schnakenburg, Long-term biocompatibility of a corrodible peripheral iron stent in the porcine descending aorta, Biomater 27 (28) (2006) 4955–4962.

[2] T. Kraus, F. Moszner, S. Fischerauer, M. Fiedler, E. Martinelli, J. Eichler, F. Witte, E. Willbold, M. Schinhammer, M. Meischel, P.J. Uggowitzer, J.F. Loffler, A. Weinberg, Biodegradable Fe-based alloys for use in osteosynthesis: outcome of an in vivo study after 52 weeks, Acta Biomater. 10 (7) (2014) 3346–3353.

[3] H. Hermawan, D. Dubé, D. Mantovani, Development of degradable Fe-35Mn alloy for biomedical application, Adv. Mater. Res. 15–17 (2006) 107–112.

[4] M. Schinhammer, A.C. Hanzi, J.F. Loffler, P.J. Uggowitzer, Design strategy for biodegradable Fe-based alloys for medical applications, Acta Biomater. 6 (5) (2010) 1705–1713.

[5] H. Hermawan, A. Purnama, D. Dube, J. Couet, D. Mantovani, Fe–Mn alloys for metallic biodegradable stents: degradation and cell viability studies, Acta Biomater. 6 (5) (2010) 1852–1860.

[6] H. Hermawan, D. Mantovani, Process of prototyping coronary stents from biodegradable Fe-Mn alloys, Acta Biomater. 9 (10) (2013) 8585–8592.

[7] E. Zhang, H. Chen, F. Shen, Biocorrosion properties and blood and cell compatibility of pure iron as a biodegradable biomaterial, J. Mater. Sci. Mater. Med. 21 (7) (2010) 2151–2163.

[8] S. Zhu, N. Huang, L. Xu, Y. Zhang, H. Liu, H. Sun, Y. Leng, Biocompatibility of pure iron: in vitro assessment of degradation kinetics and cytotoxicity on endothelial cells, Mater. Sci. Eng. C 29 (5) (2009) 1589–1592.

[9] T. Huang, Y. Zheng, Uniform and accelerated degradation of pure iron patterned by Pt disc arrays, Sci. Rep. 6 (2016) 23627.

[10] T. Huang, Y. Zheng, Y. Han, Accelerating degradation rate of pure iron by zinc ion implantation, Regen. Biomater. 3 (4) (2016) 205–215.

[11] M. Moravej, A. Purnama, M. Fiset, J. Couet, D. Mantovani, Electroformed pure iron as a new biomaterial for degradable stents: in vitro degradation and preliminary cell viability studies, Acta Biomater. 6 (5) (2010) 1843–1851.

[12] A. Orinak, R. Orináková, Z. Orsagova Kralova, A. Morovska Turonova, M. Kupková, M. Hrubovčáková, J. Radonak, R. Džunda, Sintered metallic foams for biodegradable bone replacement materials, J. Porous Mater. 21 (2014).

[13] M. Dehestani, K. Trumble, H. Wang, H. Wang, L.A. Stanciu, Effects of microstructure and heat treatment on mechanical properties and corrosion behavior of powder metallurgy derived Fe–30Mn alloy, Mater. Sci. Eng. A 703 (2017) 214–226.

[14] A. Drynda, T. Hassel, F.W. Bach, M. Peuster, In vitro and in vivo corrosion properties of new iron-manganese alloys designed for cardiovascular applications, J. Biomed. Mater. Res. B Appl. Biomater. 103 (3) (2015) 649–660.

[15] A. Atrens, M. Liu, N.I. Zainal Abidin, Corrosion mechanism applicable to biodegradable magnesium implants, Mater. Sci. Eng., B 176 (20) (2011) 1609–1636.

[16] J. Čapek, J. Kubásek, D. Vojtěch, E. Jablonská, J. Lipov, T. Ruml, Microstructural, mechanical, corrosion and cytotoxicity characterization of the hot forged FeMn30 (wt.%) alloy, Mater. Sci. Eng. C 58 (2016) 900–908.

[17] M.S. Dargusch, A. Dehghan-Manshadi, M. Shahbazi, J. Venezuela, X. Tran, J. Song, N. Liu, C. Xu, Q. Ye, C. Wen, Exploring the role of manganese on the microstructure, mechanical properties, biodegradability, and biocompatibility of porous iron-based scaffolds, ACS Biomater. Sci. Eng. 5 (4) (2019) 1686–1702.

[18] A. Gebert, F. Kochta, A. Voß, S. Oswald, M. Fernandez-Barcia, U. Kühn, J. Hufenbach, Corrosion studies on Fe-30Mn-1C alloy in chloride-containing solutions with view to biomedical application, Mater. Corros. 69 (2) (2018) 167–177.

[19] H. Hermawan, H. Alamdari, D. Mantovani, D. Dubé, Iron–manganese: new class of metallic degradable biomaterials prepared by powder metallurgy, Powder Metall. 51 (1) (2008) 38–45.

[20] H. Hermawan, D. Dube, D. Mantovani, Degradable metallic biomaterials: design and development of Fe-Mn alloys for stents, J. Biomed. Mater. Res. A. 93 (1) (2010) 1–11.

[21] B. Liu, Y.F. Zheng, Effects of alloying elements (Mn, Co, Al, W, Sn, B, C and S) on biodegradability and in vitro biocompatibility of pure iron, Acta Biomater. 7 (3) (2011) 1407–1420.

[22] R.-Y. Liu, R.-G. He, L.-Q. Xu, S.-F. Guo, Design of Fe–Mn–Ag alloys as potential candidates for biodegradable metals, Acta Metall. Sin.-Engl. 31 (6) (2018) 584–590.

[23] Q. Zhang, P. Cao, Degradable Porous Fe-35wt.%Mn Produced via Powder Sintering from NH4HCO3 Porogen, 2015.

[24] J. Čapek, K. Stehlíková, A. Michalcová, Š. Msallamová, D. Vojtěch, Microstructure, mechanical and corrosion properties of biodegradable powder metallurgical Fe-2 wt% X (X = Pd, Ag and C) alloys, Mater. Chem. Phys. 181 (2016) 501–511.

[25] J. Čapek, S. Msallamová, E. Jablonská, J. Lipov, D. Vojtěch, A novel high-strength and highly corrosive biodegradable Fe-Pd alloy: structural, mechanical and in vitro corrosion and cytotoxicity study, Mater. Sci. Eng. C 79 (2017) 550–562.

[26] M. Schinhammer, P. Steiger, F. Moszner, J.F. Loffler, P.J. Uggowitzer, Degradation performance of biodegradable Fe-Mn-C(-Pd) alloys, Mater. Sci. Eng. C 33 (4) (2013) 1882–1893.

[27] T. Huang, Y. Cheng, Y. Zheng, In vitro studies on silver implanted pure iron by metal vapor vacuum arc technique, Colloids Surf., B 142 (2016) 20–29.

[28] P. Sotoudehbagha, S. Sheibani, M. Khakbiz, S. Ebrahimi-Barough, H. Hermawan, Novel antibacterial biodegradable Fe-Mn-Ag alloys produced by mechanical alloying, Mater. Sci. Eng. C 88 (2018) 88–94.

[29] P. Sotoudeh Bagha, M. Khakbiz, S. Sheibani, H. Hermawan, Design and characterization of nano and bimodal structured biodegradable Fe-Mn-Ag alloy with accelerated corrosion rate, J. Alloys Compd. 767 (2018) 955–965.

[30] M. Wiesener, K. Peters, A. Taube, A. Keller, K.P. Hoyer, T. Niendorf, G. Grundmeier, Corrosion properties of bioresorbable FeMn-Ag alloys prepared by selective laser melting, Mater. Corros. 68 (10) (2017) 1028–1036.

[31] N.B. Sing, A. Mostavan, E. Hamzah, D. Mantovani, H. Hermawan, Degradation behavior of biodegradable Fe35Mn alloy stents, J. Biomed. Mater. Res. B Appl. Biomater. 103 (3) (2015) 572–577.

[32] M. Hrubovčáková, M. Kupková, M. Džupon, Fe and Fe-P foam for biodegradable bone replacement material: morphology, corrosion behaviour, and mechanical properties, Advances in Materials Science and Engineering (2016) 2016.

[33] Y. Feng, J. Fornell, H. Zhang, P. Solsona, M.D. Baró, S. Suriñach, E. Pellicer, J. Sort, Synthesis of α-Fe2O3 and Fe-Mn oxide foams with highly tunable magnetic properties by the replication method from polyurethane templates, Materials 11 (2) (2018).

[34] P. Sharma, P.M. Pandey, A novel manufacturing route for the fabrication of topologically-ordered open-cell porous iron scaffold, Mater. Lett. 222 (2018) 160–163.

[35] N.E. Putra, M.A. Leeflang, M. Minneboo, P. Taheri, L.E. Fratila-Apachitei, J.M. C. Mol, J. Zhou, A.A. Zadpoor, Extrusion-based 3D printed biodegradable porous iron, Acta Biomater. 121 (2021) 741–756.

[36] M. Caligari Conti, B. Mallia, E. Sinagra, P. Schembri Wismayer, J. Buhagiar, D. Vella, The effect of alloying elements on the properties of pressed and non-pressed biodegradable Fe–Mn–Ag powder metallurgy alloys, Heliyon 5 (9) (2019).

[37] M. Heiden, E. Nauman, L. Stanciu, Bioresorbable Fe-Mn and Fe-Mn-ha materials for orthopedic implantation: enhancing degradation through porosity control, Adv. Healthc. Mater. 6 (13) (2017).

[38] A. Šalak, M. Selecká, Thermodynamic conditions for the Mn–O system in sintering of manganese steels, in: A. Šalak, M. Selecká (Eds.), Manganese in Powder Metallurgy Steels, Cambridge International Science Publishing Ltd., Cambridge, 2012, pp. 5–21.

[39] M. Dehestani, K. Trumble, H. Wang, H. Wang, L. Stanciu, Effects of Microstructure and Heat Treatment on Mechanical Properties and Corrosion Behavior of Powder Metallurgy Derived Fe–30Mn Alloy, 2017.

[40] C.S. Obayi, R. Tolouei, A. Mostavan, C. Paternoster, S. Turgeon, B.A. Okorie, D. O. Obikwelu, D. Mantovani, Effect of grain sizes on mechanical properties and biodegradation behavior of pure iron for cardiovascular stent application, Biomatter 6 (2016). October 2015.

[41] S.V. Lamaka, R. Souto, M. Ferreira, In-situ Visualization of Local Corrosion by Scanning Ion-Selective Electrode Technique, SIET), 2010, pp. 2162–2173.

[42] M. Schinhammer, J. Hofstetter, C. Wegmann, F. Moszner, J.F. Löffler, P. J. Uggowitzer, On the immersion testing of degradable implant materials in simulated body fluid: active pH regulation using CO2, Adv. Eng. Mater. 15 (6) (2013) 434–441.

[43] A.J. Bard, F.R.F. Fan, J. Kwak, O. Lev, Scanning electrochemical microscopy. Introduction and principles, Anal. Chem. 61 (2) (1989) 132–138.

[44] S.V. Lamaka, O.V. Karavai, A.C. Bastos, M.L. Zheludkevich, M.G.S. Ferreira, Monitoring local spatial distribution of Mg2+, pH and ionic currents, Electrochem. Commun. 10 (2) (2008) 259–262.

[45] L. Shabala, T. Ross, I. Newman, T. McMeekin, S. Shabala, Measurements of net fluxes and extracellular changes of H+, Ca2+, K+, and NH4+ in Escherichia coli using ion-selective microelectrodes, J. Microbiol. Methods 46 (2) (2001) 119–129.

[46] J.G. Ummadi, C.J. Downs, V.S. Joshi, J.L. Ferracane, D. Koley, Carbon-based solid-state calcium ion-selective microelectrode and scanning electrochemical microscopy: a quantitative study of pH-dependent release of calcium ions from bioactive glass, Anal. Chem. 88 (6) (2016) 3218–3226.

[47] L. Shabala, T. Ross, T. McMeekin, S. Shabala, Non-invasive microelectrode ion flux measurements to study adaptive responses of microorganisms to the environment, FEMS Microbiol. Rev. 30 (3) (2006) 472–486.

[48] S.V. Lamaka, J. Gonzalez, D. Mei, F. Feyerabend, R. Willumeit-Römer, M. L. Zheludkevich, Local pH and its evolution near Mg alloy surfaces exposed to simulated body fluids, Advanced Materials Interfaces 5 (18) (2018) 1800169.

[49] D. Mei, C. Wang, S.V. Lamaka, M.L. Zheludkevich, Clarifying the influence of albumin on the initial stages of magnesium corrosion in Hank's balanced salt solution, Journal of Magnesium and Alloys (2020), https://doi.org/10.1016/j.jma.2020.07.002.

[50] D. Mei, S.V. Lamaka, J. Gonzalez, F. Feyerabend, R. Willumeit-Römer, M. L. Zheludkevich, The role of individual components of simulated body fluid on the corrosion behavior of commercially pure Mg, Corrosion Sci. 147 (2019) 81–93.

[51] F. Ferreira, G. Luxardi, B. Reid, L. Ma, V. Raghunathan, M. Zhao, Real-time physiological measurements of oxygen using a non-invasive self-referencing optical fiber microsensor, Nat. Protoc. 15 (2) (2020) 207–235.

[52] E.L. Silva, S.V. Lamaka, D. Mei, M.L. Zheludkevich, The reduction of dissolved oxygen during magnesium corrosion, ChemistryOpen 7 (8) (2018) 664–668.

[53] D. Mei, S.V. Lamaka, X. Lu, M.L. Zheludkevich, Selecting medium for corrosion testing of bioabsorbable magnesium and other metals – a critical review, Corrosion Sci. 171 (2020) 108722.

[54] C. Wang, D. Mei, G. Wiese, L. Wang, M. Deng, S.V. Lamaka, M.L. Zheludkevich, High rate oxygen reduction reaction during corrosion of ultra-high-purity magnesium, npj Materials Degradation 4 (1) (2020).

[55] M.G. Taryba, M.F. Montemor, S.V. Lamaka, Quasi-simultaneous mapping of local current density, pH and dissolved O2, Electroanalysis 27 (12) (2015) 2725–2730.

[56] D. Snihirova, M. Taryba, S.V. Lamaka, M.F. Montemor, Corrosion inhibition synergies on a model Al-Cu-Mg sample studied by localized scanning electrochemical techniques, Corrosion Sci. 112 (2016) 408–417.

[57] L. Wang, D. Snihirova, M. Deng, C. Wang, B. Vaghefinazari, G. Wiese, M. Langridge, D. Höche, S. Lamaka, M.L. Zheludkevich, Insight into physical interpretation of high frequency time constant in electrochemical impedance spectra of Mg, Corrosion Sci. 187 (2021) 109501.

[58] C. Tonna, C. Wang, D. Mei, S.V. Lamaka, M.L. Zheludkevich, J. Buhagiar, Biodegradation behaviour of Fe-based alloys in Hanks' balanced salt solutions: Part I. Material characterisation and corrosion testing, Bioact. Mater. (2021), https://doi.org/10.1016/j.bioactmat.2021.05.048.

[59] Chemical equilibrium diagrams. https://www.kth.se/che/medusa/, 2020.

[60] M.S. Dargusch, J. Venezuela, A. Dehghan-Manshadi, S. Johnston, N. Yang, K. Mardon, C. Lau, R. Allavena, In vivo evaluation of bioabsorbable Fe-35Mn-1Ag: first reports on in vivo hydrogen gas evolution in Fe-based implants, Adv Healthc Mater 10 (2) (2021), e2000667.